CHALMERS

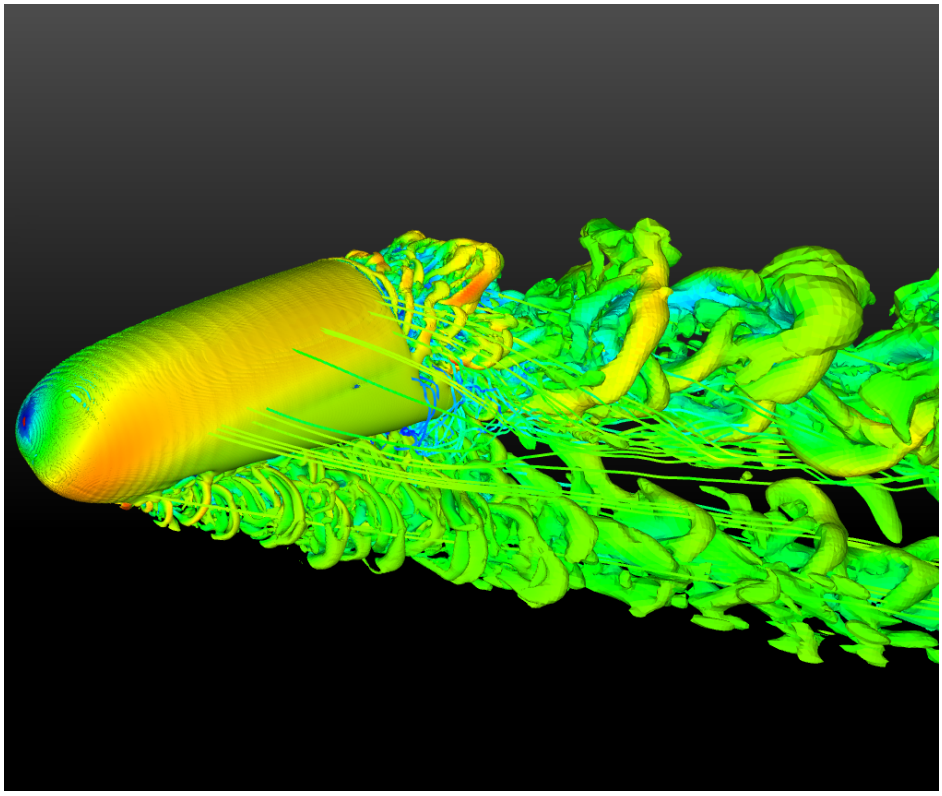

Large Eddy Simulation of a Simplified Car Model Exposed to an Unsteady Harmonic Crosswind

Master's Thesis in Solid and Fluid Mechanics

MIGUEL BRAVO

Department of Applied Mechanics
Division of Fluid Mechanics
CHALMERS UNIVERSITY OF TECHNOLOGY
Göteborg, Sweden 2014
Master's Thesis 2014:29

MASTER'S THESIS 2014:29

Large Eddy Simulation of a Simplified Car Model Exposed to an Unsteady Harmonic Crosswind

Master's Thesis in Solid and Fluid Mechanics

MIGUEL BRAVO

Department of Applied Mechanics
Division of Fluid Mechanics
CHALMERS UNIVERSITY OF TECHNOLOGY

Göteborg, Sweden 2014

Large Eddy Simulation of a Simplified Car Model Exposed to an Unsteady Harmonic Crosswind
MIGUEL BRAVO

Master's Thesis 2014:29
ISSN 1652-8557
Department of Applied Mechanics
Division of Fluid Mechanics
Chalmers University of Technology
SE-412 96 Göteborg
Sweden
Telephone: + 46 (0)31-772 1000

Cover:
some over caption

Chalmers Reproservice
Göteborg, Sweden 2014

Large Eddy Simulation of a Simplified Car Model Exposed to an Unsteady Harmonic Crosswind
Master's Thesis in Solid and Fluid Mechanics
MIGUEL BRAVO
Department of Applied Mechanics
Division of Fluid Mechanics
Chalmers University of Technology

Abstract

Large Eddy Simulation (LES) is used to simulate a case where a simplified model of a car is oscillating on its vertical axis inside a wind tunnel. This is done in order to represent incoming oscillating wind. This airflow reaches the model with an angle varying between 10 and 30 degrees. The simulation is performed for three different oscillation frequencies: 1, 2 and 4 Hz. The mesh is dynamically deformed for each timestep of the simulation in order to obtain a better description on the flow than using a quasy-steady approach, such as the ability to detect hysteresis effects. Then the evolution of the overall side force coefficient and yawing moment coefficient for the model are plotted and compared to experimental data obtained in the University of Tolouse. The differences are analyzed and recommendations for future studies and simulations are made. The computational mesh used in the simulations was created with the software FAME Hexa and the simulations were run using AVL Fire.

Keywords: Computational Fluid Dynamics (CFD), AVL FIRE, Large Eddy Simulation (LES), Oscillating Wind, Turbulence model, Dynamic Mesh Deformation

Preface

In this study a flow around an oscillating car model was simulated using Large Eddy Simulation for three different oscillation frequencies. FAME Hexa was used for mesh creation and simulation were run on AVL FIRE. The work of this thesis has been carried out from August 2013 to February 2014 at the Department of Applied Mechanics, Division of Fluid Dynamics at Chalmers University of Technology (Gteborg, Sweden). The thesis was supervised by Professor Sinisa Krajnović.

Acknowledgments

I would like to thank Sinisa Krajnović for his supervision at Chalmers, as my well as my supervisor in Universidad Politica de Madrid, Jorge Muñoz. I would also like to thank Jan Östh for helping me with a lot with practical issues when dealing with mesh building, simulation settings and CFD knowledge in general. I also want to acknowledge Anders Bengtsson for his help with the dynamic deformation of the mesh. I also want to thank the people in the AVL office in Maribor for taking me in for two days and helping me greatly with my understanding of their mesh creating tool FAME Hexa. I would like to thank the Swedish National Infrastructure for Computing (SNIC) for allowing me access to their systems. I also want to thank Monica Vargman for helping me with different administrative issues. Finally, I would like to thank my family for showing real interest in what my work was about and for their support, and also my friends in Spain and Sweden who already went through their Master's Thesis for their valuable advice.

Göteborg March 2014
Miguel Bravo

Nomenclature

Abbreviations

CFL	Courant Friedichs Lewis
PANS	Partially Averaged Navier-Stokes
URF	Underrelaxation factor
LES	Large Eddy Simulation

Magnitudes

$\triangle$x,$\triangle$y,$\triangle$z	Cell dimensions
n^+	Wall unit, normal direction
n	Wall normal distance
u_*	Friction velocity
τ_w	Surface shear stress
$\bar{u}$	Resolved filtered velocity
$\bar{p}_i$	Resolved filtered pressure
τ_{ij}	Sgs stress tensor
v_{sgs}	Sgs viscosity
S_{ij}	Resolved rate-of-strain tensor
l	Length scale
C_s	Smagorinsky constant
$\triangle$	Filter width
f	Oscillation frequency
$f*$	Reduced frequency
F_y	Side force
L_{ref}	Overall model length
M_z	Yawing moment (model coordinates system)
S_{ref}	Model frontal area
U_0	Free-stream velocity
C_n	Yawing moment coefficient
C_y	Overall side force coefficient
Re	Reynolds number
v	Air kinematic viscosity

Contents

Chapter 1

Introduction

1.1 Background

Road vehicles are more often than not subjected to unsteady flows. These can be caused by several reasons: wind gusts, irregular terrain around the road, overtaking or the passage of two or more vehicles. This unsteadiness can also be produced by the interaction of vertical forces and the suspension movement of the vehicle itself. The fact that the curvature of the vehicle often leads to variable separation positions also contributes to the unsteadiness of the flow. All these factors produce a time-dependant flow that is much more difficult to predict and thus creates uncertainty in how the aerodynamic forces and moments develop.

Since a flow with unsteady conditions is much more difficult to simulate (both with wind tunnel experiments and numerical simulations), usually a 'quasi-static' approach is taken. This means the conditions are changed in a non-continuous way, taking each position as a single simulation case. Although the whole array of positions is studied this way, the reality of the flow conditions is being modified, and this has a significant effect on the results and produces inaccurate predictions in forces and moments.

These differences between methods are expected to be a result of the lag in the response of the flow to the changes in the boundary conditions, which produces effects such as hysteresis and phase shift in force.

1.2 Previous work

In 1967, Beauvais [2] performed some experimental tests that showed differences between real transient flow and and quasi-steady conditions. Even an study such based on the slender body theory by Hucho and Emmelmann [11] revealed discrepancies in forces and moments due to transient effects. These differences between prediction and reality were also observed by Garry and Cooper [6], in an experiment with simple rectangular prisms rotating around its base when on a steady flow. Drag and yawing moment weren't significantly affected, but the aerodynamic coefficient in the dynamic test and the equivalent in the static experiment were displaced relative to the yaw angle (the phenomenom of 'phase-shift' was taking place).

When comparing the forces and moments on a one-box vehicle in steady flow conditions and in a wind gust, Kobayashi and Yamada [12] found that the peak yawing moment was twice as large in the second case. Dominy and Ryan [4] used a different approach for their experiments, using a second jet in an open jet wind tunnel to direct the wind gust, and thus changing the boundary conditions instead of changing the vehicle position, similarly to Krajnovic [13] and Hemida and Krajnovic [10] when studying the influence of wind

gust on trains and buses using detached eddy simulations. No change in yawing moment was found between transient and steady simulation by Ryan and Dominy [4] when using a second jet, so there's an obvious difference compared to the situation when the vehicle is moving.

A good example of the hysteresis effect mentioned earlier is the study by Gillin et al. [7], where a body shaped as a cylinder with its front shaped as a Rankine half-oval and its rear base inclined oscillated around an horizontal axis. Passmore and Mansor [15] also found great differences between dynamic and quasi-static test when constraining the body to oscillate in a single degree of freedom.

The simplified vehicle shape studied in this thesis was analyzed by Guilmineau and Chometon [9] using RANS and a $\kappa - \omega$ SST model. This simulation successfully captured the trends in the surface pressure path during the model rotation, although RANS simulation failed to give a good description of the complicated flow processes in the wake of the model. That same shape was studied in a quasi-steady approach using DES by Guilmineau et al. [8] and with LES by Krajnovic and Sarmast [14], showing that LES is a better solution for the flow around this body.

1.2.1 Description of the Ferrand, V. and Gorchal, B. experiment

In the experimental setup by Vale Ferrand and Bartolomiej Gorchal [5], the model shown in 1.2.1 , referred as "Willy", is placed in an oscillating yaw device with an amplitude of yaw angle of $\triangle\beta$=20. The frequency can be adjusted from an almost quasi-static movement (0.2 Hz) to the following cases: 1 Hz, 2 Hz and 4 Hz.

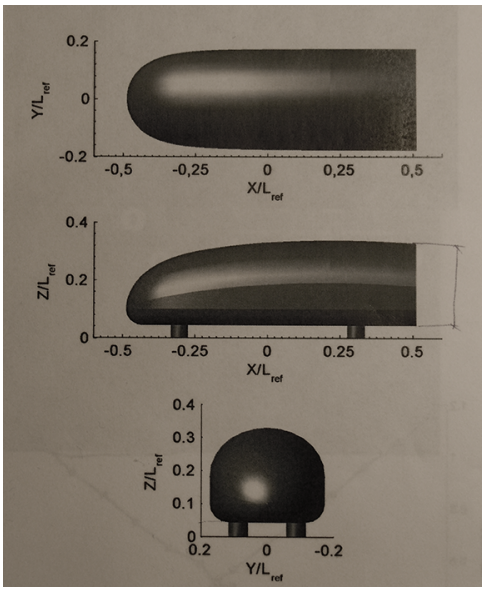

Figure 1.2.1: 'Willy' model used in the experimental setup.

This rotating model is positioned on a wind tunnel whose test section has a square cross-section of 0.45 by 0.45 m, and a length of 0.7 m. The upstream average velocity is 21 m/s, that corresponds to a Reynolds number $Re = 3.7 * 10^5$, based on the model length (0.28 m). Although this Reynolds number is lower than the one around ground vehicles, the physical mechanisms were expected to give good elements for interpretation full scale cases. The turbulence level at the center of the test section is 2%, and the free stream velocity and turbulence intensity show a maximum spatial deviation of 1% and 0.5 % respectively. In order to reduce the boundary layer, the turntable where the model

stands is elevated, giving a measured thickness of the boundary layer of $\delta_{99\%} = 6$ mm at 0.41 Lref downstream from the leading edge, with a boundary layer shape factor of 1.31.

The references system are described in 1.2.1. The yaw angle is positive when the upstream wind comes from the side of positive y (referred as windward).

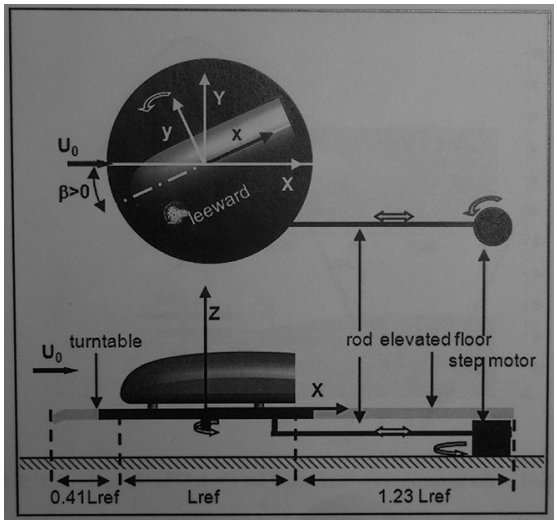

Figure 1.2.2: Model with reference system and dimensions.

In the experiment, two different angular ranges were studied: -10<β<10, and 10<β<30.

The experimental results for the total side force coefficient and the yawing moment coefficient are shown in 1.2.4 and 1.2.3. The red straight line in each of the graphs represent the results for the static experiment, where the model was rotated at quasiestatic frequencies. Subsequent loops represent the values for oscillations of 1, 2 and 4 Hz respectively.

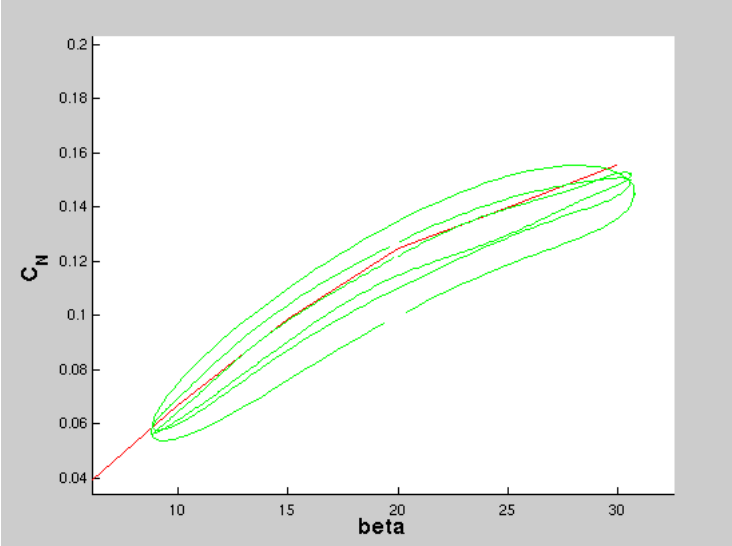

Figure 1.2.3: Yawing moment coefficient obtained for the experimental setup.

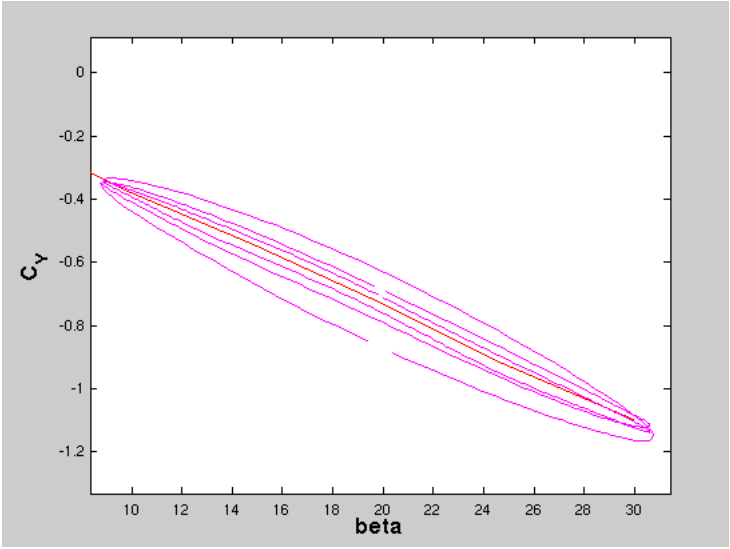

Figure 1.2.4: Total side force coefficient obtained for the experimental setup.

1.3 Goal of the study

This thesis is based on the experiment described in 1.2.1. That same configuration is reproduced using CFD, and more specifically LES (Large Eddy Simulation) as a turbulence model and dynamic mesh deformation at each timestep as a way to simulate the rotation of the body (instead of several static simulations, one for each position). The simulations are performed for three frequencies: 1, 2 and 4 Hz. A good sdescription of the flow is expected to be obtained, including dynamic effects not present in similar quasistatic studies.

The final goal of the thesis is to obtain the values for the side force coefficient and yawing moment coefficient in several cycles and compare them to the experimental values. The coincidence or not of these results will be studied in order to evaluate the validity of this simulation procedure for this kind of studies.

1.4 Limitations

The mesh will be produced using only FAME Hexa. Using a more manual approach such as ICEM could result in a better mesh, but it was considered too time consuming. Time and hardware limitations also restricted the available running time as well as the number of cells of the computational grid. Also, the quasiestatic frequency case (0.2 Hz) was not resolved due to the time required to get several cycles simulated.

1.5 Contents

In this section a brief summary of the contents of each chapter is presented.

In the theory chapter the basis of numerical simulation for fluid mechanics are described, and the two different turbulence models (LES and PANS) used in the thesis are explained. The resolution requirements for the mesh are also mentioned.

The procedure chapter explains the steps taken to prepare and run the simulations. It is described how the initial given geometry was modified to adapt it to the proposed study. This geometry, formed by surfaces and edges, is then used to generate the mesh using the

software FAME Hexa, in a manner which is also described in that chapter. Once the mesh is created, the steps taken to configure the simulation in AVL Fire are detailed.

The next chapter presents the results of the different simulations performed, starting by analysing the resolution requirements. Then the flow is visualized in several figures and the dynamic effects that can be observed explained. The values of the force and moment coefficients are compared with the experimental data. Additionally, the results of two secondary simulations made in order to evaluate the influence of the dynamic mesh deformation are discussed.

Finally, the last chapter presents a series of conclusions that summarize the findings of the thesis. The difference between experimental and simulation results are evaluated, and also the numerical quality of the simulations and the possible extensions of the study.

Chapter 2

Theory

2.1 Navier-Stokes equations and RANS

The Navier-Stokes equations are used to describe the motion of viscous fluids. They are a result of the Newton laws of motion combined with the assumption of fluid stress being the sum of a diffusing viscous term and a pressure term.

For incompressible flow and tensor notation, the Navier-Stokes equations can be expressed as:

$$\rho(\frac{\partial u_i}{\partial t} + u_j\frac{\partial u_i}{\partial x_j}) = -\frac{\partial p}{\partial x_i} + \mu\frac{\partial^2 u_i}{\partial x_j \partial x_j} + f_i \tag{2.1.1}$$

Where f represents forces such as gravity or centrifugal, and

$$\mu\frac{\partial^2 u_i}{\partial x_j \partial x_j} \tag{2.1.2}$$

is derived from the shear stress term for incompressible fluids.

These equations can be decomposed in time-averaged and fluctuating variables, in order to be able to resolve them for turbulent flows. Using the 'Einstein notation', the Reynolds-averaged Navier-Stokes equations (RANS) are derived as:

$$\rho\bar{u_j}\frac{\partial\bar{u_i}}{\partial\bar{x_j}} = \rho\bar{f_j} + \frac{\partial}{\partial x_j}(-\bar{p}\delta_{ij} + \mu(\frac{\partial\bar{u_i}}{\partial x_j} + \frac{\partial\bar{u_j}}{\partial x_i}) - \rho\overline{u_i' u_j'}) \tag{2.1.3}$$

The left side is representative of the change in mean momentum due to the unsteadiness and convection in the mean flow. The right side represents the mean body forces, the isentropic stress due to pressure, viscous stress and finally the apparent stress (Reynolds stress, $-\rho\overline{u_i' u_j'}$).

2.2 Turbulence models

Turbulence, as a chaotic behaviour of flow in time-dependent problems, is a result of inertia and accelerations in a fluid. A turbulent flow has a hierarchy of scales (in length, velocity and time), where large scales (large eddies) decay and transfer its energy to smaller scales, where eventually the kinetic energy is dissipated at the denominated Kolmorogov scales, where the viscous effects are dominant over inertial effects.

Solving turbulent Navier-Stokes equations is a difficult problem since the flow is composed of many different mixing scales. Trying to solve all scales (Direct Numerical Simulation) is technically not feasible due to the mesh resolution required for it.

This is the reason why turbulence models, along with the Reynolds-averaged Navier-Stokes equations are used to solve problems in computational fluid dynamics. Turbulence models predict the effect of turbulence, representing the scales that are not being resolved in different ways.

2.3 Large Eddy Simulation (LES)

LES is a mathematical turbulence model which reduces the range of length scales of the solution by applying 'low pass filtering' to the Navier-Stokes equations, eliminating the small scales and thus reducing the computational cost of the simulation.

Denoting the resolved filtered velocity and pressure as $\bar{u}_i$ and $\bar{p}_i$, the governing equations for LES are:

$$\frac{\partial \bar{u}_i}{\partial t} + \frac{\partial}{\partial x_j}(\bar{u}_i \bar{u}_j) = -\frac{1}{\rho}\frac{\partial \bar{p}}{\partial x_i} + v\frac{\partial^2 \bar{u}_i}{\partial x_j \partial x_j} - \frac{\partial \tau_{ij}}{\partial x_j} \tag{2.3.1}$$

and

$$\frac{\partial \bar{u}_i}{\partial x_i} = 0 \tag{2.3.2}$$

The SGS stress tensor, $\tau_{ij} = \overline{u_i u_j} - \bar{u}_i \bar{u}_j$contains the influence of the small scales on the large energy scales in 2.3.1. The original eddy viscosity model proposed by Smagorinsky [16] will be used for its simplicity and lower computational cost. This method assumes that dissipation and energy production of the small scales are balanced. According to said model, the anisotropic part of the SGS stress sensor is represented as:

$$\tau_{ij} - \frac{1}{3}\delta_{ij}\tau_{kk} = -2v_{sgs}\bar{S}_{ij} \tag{2.3.3}$$

with: $v_{sgs} = (C_s f \triangle)^2 \left|\bar{S}\right|$being the SGS viscosity, and S_{ij}

$$S_{ij} = \frac{1}{2}\left(\frac{\partial \bar{u}_i}{\partial x_j} + \frac{\partial \bar{u}_j}{\partial x_i}\right) \tag{2.3.4}$$

is the resolved rate-of-strain tensor, being $\left|\bar{S}\right| = (2\bar{S}_{ij}\bar{S}_{ij})^{\frac{1}{2}}$, and f is the van Driest damping function:

$$f = 1 - exp\left(\frac{n^+}{25}\right) \tag{2.3.5}$$

where n is the wall normal distance.This function allows to partially take in account the wall effects by damping length scale $l = C_s\triangle$ near the walls. The value of $c = 0.1$ is used in this thesis. Filter width $\triangle$ is defined as $\triangle = (\triangle_1\triangle_2\triangle_3)^{\frac{1}{3}}$, where 1,2,3 refers to the computational cell size in the three coordinate directions.

2.4 Partially Averaged Navier-Stokes (PANS)

Although the main model used in this study is LES, one secondary simulation with PANS was also performed (see 4.4), so brief description of it is in order.

PANS is a model designed to bridge between RANS (Reynolds Averaged Navier-Stokes, where all turbulent scales are modeled) and DNS (Direct Numerical Simulation, for which all scaled are resolved), so only some scales are modeled according to RANS-to-DNS ratio that gradually changes, creating a smooth transition. This parameter is calculated for every point at the end of each timestep of the simulation.

2.5 General considerations for mesh creation

When creating a mesh for CFD simulations, there are some quantities and coefficients that should be studied beforehand.

Viscous unit, denoted n^+, is a dimensionless quantity calculated as:

$$n^+ = \frac{u_* n}{\nu} \tag{2.5.1}$$

with n being the normal distance to the surface and u_* the friction velocity, obtained from the surface shear stress τ_w as:

$$u_* = \sqrt{\frac{\tau_w}{\rho}} \tag{2.5.2}$$

The minimum wall-node distance for the closest cell to the wall, in order to resolve boundary layers, must verify $n^+ < 1$.

LES and PANS simulations also have strict requirements related to the viscous units in the stream wise direction (l) and the direction perpendicular to both the normal and stream wise direction (s), being those viscous units defined as:

$$s^+ = \frac{n_+ s}{n} \tag{2.5.3}$$

$$l^+ = \frac{n_+ l}{n} \tag{2.5.4}$$

The resolution requirements for LES and PANS, in order for the turbulent scales to be adequately resolved, are as follows [3]:

Unit	Requirement for LES	Requirement for PANS
n^+	< 1	< 1
s^+	< 30	< 100
l^+	< 100	< 200

Table 2.5.1: Resolution requirements for LES in term of wall units

Note that a consequence of this requirements is that a mesh used for LES is always good enough for a PANS simulation, although it could be optimised to have fewer cells and require thus less computational resources.

On the other hand, when performing unsteady simulations, the time step size is limited according to the CFL number being smaller than one:

$$CFL = \frac{U \triangle t}{\triangle x} \leq 1 \tag{2.5.5}$$

This represents that a particle of the fluid must not travel through more than one cell during on timestep. However, it is sometimes acceptable to exceed these values if it is in small specific areas in the flow, since most implicit solvers are able to converge even when a low percentage of cells don't meet this requirement [1].

Chapter 3

Procedure

3.1 Introduction

In this chapter the steps leading to configuring a successful simulation are described. Firstly, the given geometry was analysed and modified accordingly to the requirements of the study. Then a mesh was generated from it using FAME Hexa, a software whose characteristics are also described. The dynamic mesh deformation is then discussed. Finally, the main parameters defined for the simulation are described.

3.2 Geometry

A scaled up version of the studied geometry was provided as data. This geometry had to be modified in several ways in order to apply for the studied case.

First of all, a new selection for the model and the road directly under it was created. This selection was then rotated -20, around the rotating axis at x=0.33 m and y =0, since this is the starting and central position of the model for the studied cases. This way, not only is the mesh undeformed in the first timesteps, which is good for convergence, but also the deformation of the mesh at the extreme positions (10 and 30) will be smaller compared to the hypotetical case of building the mesh at 10 and then deforming it up to 30.

At first, a real-scale mesh was built for the simulations, downscaling the given geometry. However, this proved to be a bad decision, since using the actual oscillating frequency instead of an equivalent lower one for a larger model required a faster deformation of the mesh and lead to convergence problems that didn't appear in the larger mesh. Thus the upscaled mesh was chosen.

However, the given geometry had to be further modified. The width of the wind tunnel at the size of the experiment would interfere with the mesh deformation, since the mesh deformation algorithm produces a deformed cylindrical area around the model that would intersect with the wind tunnel walls. In order to increase the width for our case, it had to be studied first if the experimental setup presented a very deformed flow around the body due to the presence of walls (blocking). If that were the case, increasing the dimensions of the tunnel could affect the results significantly. The blocking factor $\frac{A_2}{A_1}$ (where A_2 is the cross section area and A_1 is the projected vehicle area) turned out to be around 6%, which was considered low enough to assume that increasing the width of the wind tunnel has no significant effect on the results. The blocking factor was calculated the projected image of the model in the direction of the flow in AVL Workflow Manager. This image was then transformed to black and white color mode in Adobe Photoshop, which can then be used to exactly calculate the percentage of black to white area.

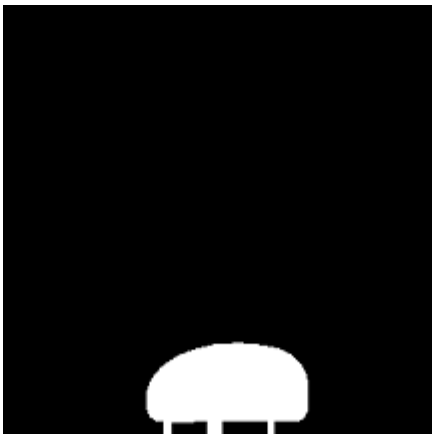

Figure 3.2.1: Picture used to determine the blocking factor

The final width of the cross section was set at 1.6 m, mantaining 1.45 m as its height. The total length of the wind tunnel was set at 7.4 meters, which was deemed enough to avoid error in the outlet of the wind tunnel, which shouldn't receive turbulence form the model's wake.

3.3 Mesh creation

The mesh used for calculations was produced with the software AVL Fire FAME Hexa, and then deformed dynamically for each timestep with a formula set in Fire Workflow Manager.

3.3.1 Fundamentals of FAME Hexa

Fire FAME Hexa is an automated mesh generator, which produces and refines meshes from a surface and several used defined input parameters. Edge data can also be added as input for hard edges in order to avoid smoothing and to be able to specify refinements around said edges. This software also generates boundary layers (either in every wall or in specific regions) by specifying its number, final thickness and growth ratio.

The process by which the mesh is created is shown in the figures below. First, an initial bounding box (black rectangle in 3.3.1) is created around the geometry, which is then subdivided and refined around the surface (red grid). Further refinement produces the first mesh (3.3.2)

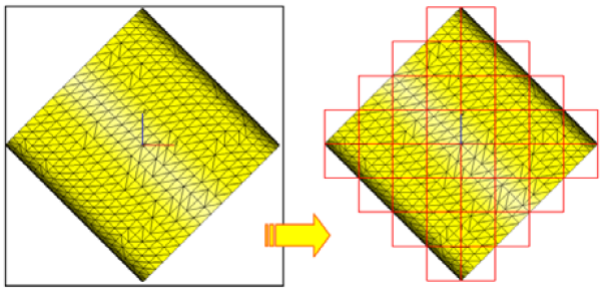

Figure 3.3.1: Refining of bounding box in FAME Hexa

After the initial grid has been produced, it must be projected over the surface. Providing an edge file that contains all relevant edges allows the meshes to conserve them when the

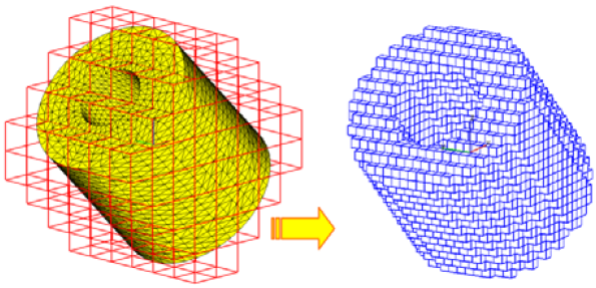

Figure 3.3.2: Initial mesh creation in FAME Hexa

projection is done. Once the projection is done, the grid is ready to have boundary layers added, as specified by the user. Then the mesh is checked for several kinds of problems (the most common being the production of cells with partially negative volume), and several algorithms are run in order to correct them.

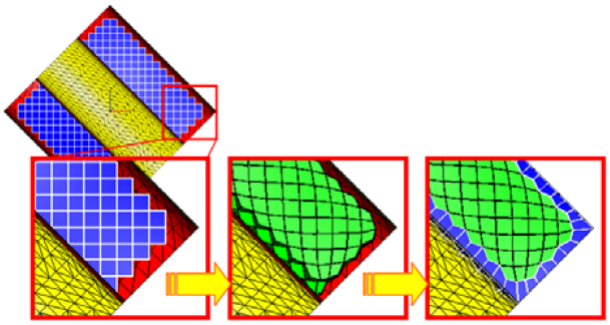

Figure 3.3.3: Projection of the initial grid and preparation for boundary layer creation.

This automated approach to mesh generation has several advantages and disadvantages when compared to more manual applications such as ICEM CFD.

Its positive aspects:

- Less time-consuming in general.
- Good mesh quality for not very complicated input surfaces.
- Enough tools to ensure good cell size continuity and appropriate boundary layers.

On the other hand:

- Lack of precise control of the mesh properties in problematic areas.
- When using complicated (e.g. detailed and realistic) surfaces, producing a mesh without negative cells can be very difficult.
- When the result is an invalid or bad quality mesh, the whole mesh has to be created again.
- It's difficult to identify which options or parameters are badly affecting the mesh (the software is a 'black box').
- Surface selections sometime lose their soft boundaries after refinement. This should be always checked after the mesh is completed.

With this particular geometry, most meshing problems presented in the connection of the holdings with the main body of the model. This area requires a good refinement, and FAME Hexa seemed to have problems avoiding creating negative cells in the cilinder-plane intersection area.

3.3.2 Mesh design

Building an appropriate mesh is an iterative process, since some parameters must be adjusted according to the results of the simulation (e.g, high velocities in a local area might require a better refinement there in order to avoid the resolution to be good enough). The parameters presented here are the result of several of these iterations, and it was considered a good compromise between quality and available computational resources and time.

- Maximum cell size: 0.029 m. This parameter sets the initial maximum dimension of each cell, before any refining is done. This is not enough to ensure a CFL number below one in all cells, but reducing this value further increases the cell count very rapidly.
- Edges: FAME Hexa allows to include an edge file along with the surface file. This avoids unintended smoothing on hard edges and also allows to specify edge-related refinements. For this case, the edges extracted in Workflow Manager and included as input were (3.3.2):
  - Intersections of the cilindrical holdigs with the car body and the floor.
  - Rear edge of the car model.
  - Edges of the wind tunnel itself.

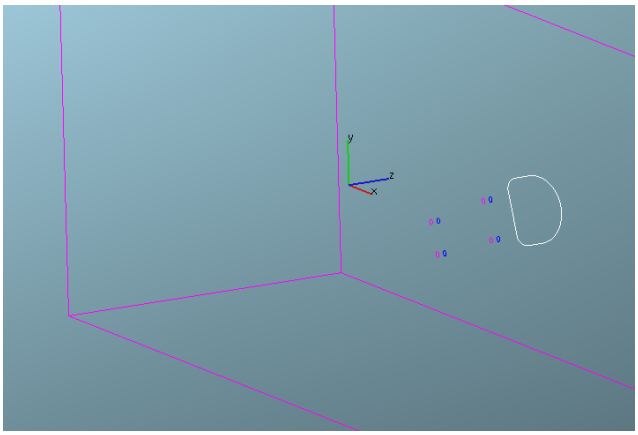

Figure 3.3.4: Edges imported into FAME Hexa.

- Default boundary layers: specifies how the cells adapt their size near the walls. By default it's set to three boundary layers with a compression ratio of 1.2, but this was be changed for specific areas as explained below.
- Box refinements: in areas where a better resolution is expected to be required, cells can be split in half in each dimension, one or several times (refinement level). In this case, four refinements levels are specified, from 1 to 4, corresponding to boxes around the body that are more refined the smaller they are.

- Refinements: refinement levels can also be specified around a face selection. This option in used in this case to further refining around the model.
- Edge refinements: the higher level of refinement of this mesh (level 6) is specified to be around the rear edge of the model.
- Boundary layers: in order to obtain the required resolution close to the walls, the boundary layers are specified in detail around the car and holdings. The thickness of the layer closest to the wall is set at 0.00002 m, and it is achieved by creating ten layers of cells that are compressed with a ratio of 1.15 each time.

The resulting mesh has 16 million cells, and the effect of the refinements can be appreciated in 3.3.2 and 3.3.2

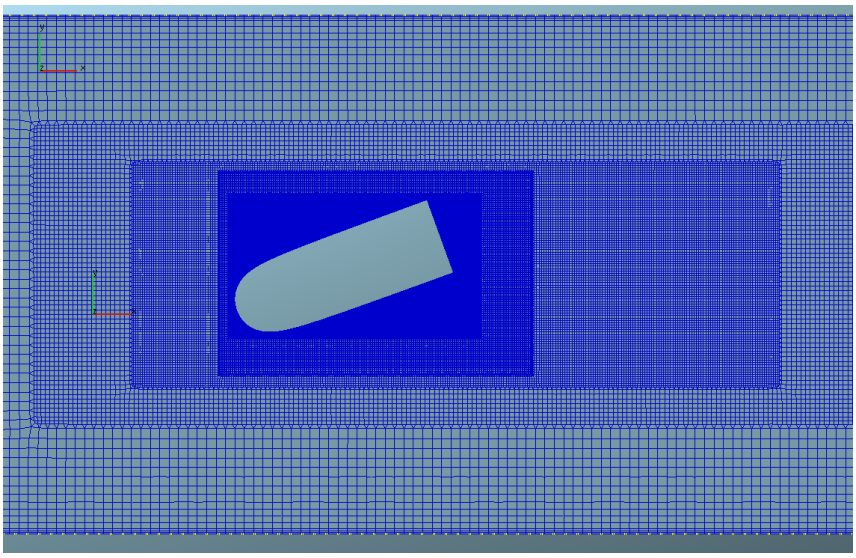

Figure 3.3.5: Detail of a Z-cut of the final mesh.

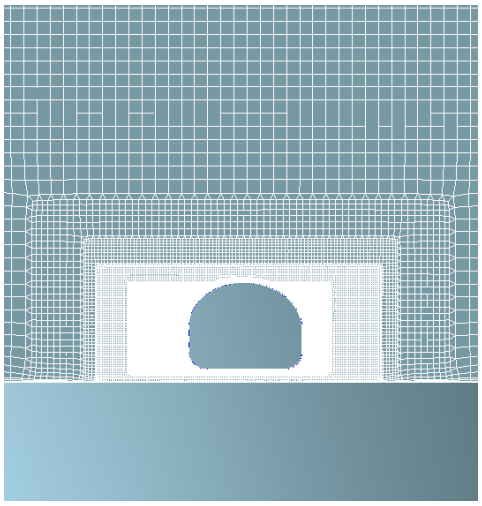

Figure 3.3.6: Detail of an X-cut of the final mesh.

3.4 Dynamic mesh deformation

In order to simulate the oscillating wind, the model will be rotated with a constant frequency between 10 and 30. The geometry of the model must be rotated as a solid object,

and then the mesh surrounding it will be rotated in decreasing amount as it gets farther away from the model.

The results of this method are visualised in 3.4.1,3.4.2 and 3.4.3. Note that, in order to get a clear visualisations, a coarse test mesh is showed in this case. This mesh was never used for calculations and its only objective was to be able to make fast and clear tests on how the mesh deformation formula worked.

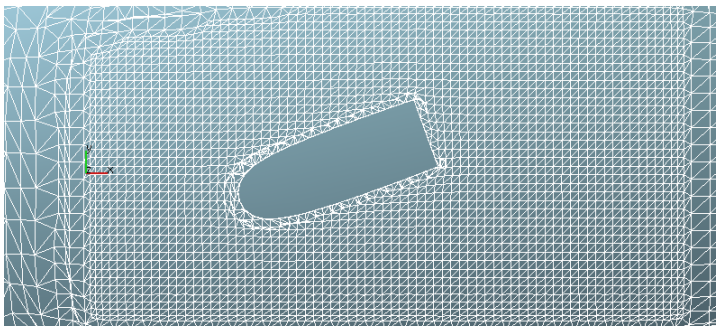

Figure 3.4.1: Z-section of the mesh when undeformed.

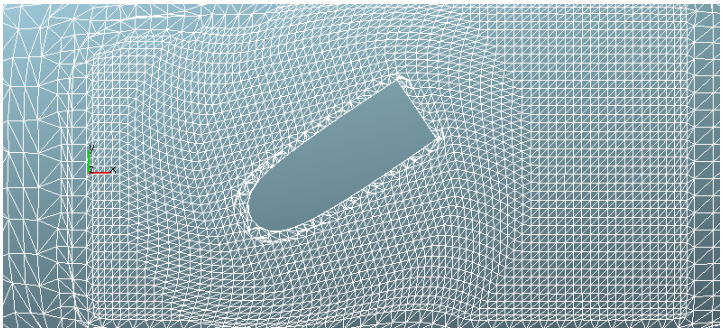

Figure 3.4.2: Z-section of the mesh when rotated.

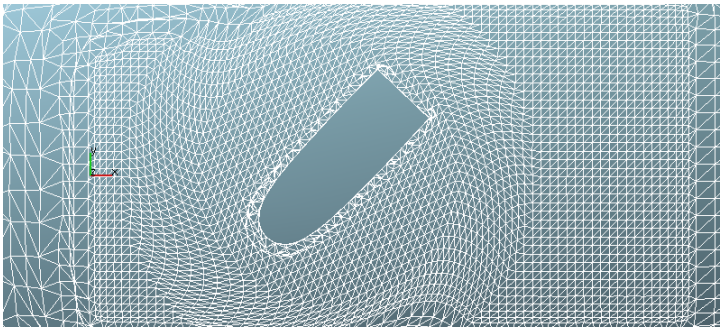

Figure 3.4.3: Z-section of the mesh with further rotation.

This provides the transient boundary conditions that the study requires, just like the experiment. However, the modification of cells on each timestep will cause problems of convergency, especially for higher frequencies. The fact that the mesh is deformed faster close to the surface, where most meshing problems arise in the static mesh by itself, is an additional problem.

The undeformed mesh is built with the model at 20 in order to avoid extreme deformations during the oscillation cycle. The model in this mesh will then oscillate around that midpoint with the given frequency. The code used is show in Annex I.

3.5 Numerical method

As stated previously, simulation will be running the LES (Large Eddy Simulation) transient model. The solver used was AVL Fire, and the same mesh was used for the three different frequencies taken into account.

3.5.1 Boundary conditions

The boundary conditions for the simulation were specified using the different surface selections of the geometry. Note the inlet velocity has been changed from 21 m/s to the equivalent one for the upscaled geometry.

Boundary	Specification
Inlet	Normal velocity equal to 8.8888 m/s
Outlet	Pressure gradient = 0
Floor (turntable)	Velocity = 0
Rest of wind tunnel	Symmetry
Car model	Velocity = 0

Table 3.5.1: Boundary conditions

3.5.2 Initial conditions

The initial conditions for the fluid (air) are set in all the domain to be 100 kPa and 8.8888 m/s, in order to accelerate convergence.

3.5.3 Main simulation parameters

In this section some of the main values that have to be specified for the simulation are detailed. Note the three frequencies used are equivalent to the original 4, 2 and 1 Hz for the original dimensions.

Timestep

The chosen timesteps are 0.0002 for 0.716 Hz; 0.0004 for 0.358 Hz,and 0.0008 for 0.179 Hz. These were limited due to the available time and computational resources.

Compressibility

The fluid (air) is considered incompressible, since the maximum velocities present in this problem are much lower than the Mach number.

Scheme order

A second order scheme is chosen for its precision.

Momentum differencing scheme

Central differencing with blending factor of 0.83 (lower than one increases the error but reduces unphysical oscillations).

Continuity differencing scheme

Central differencing with blending factor of 1

Algorithm

The algorithm used is the one used in AVL Fire by default, Semi-Implicit Method for Pressure Linked Equations (SIMPLE)

Underrelaxation factors

Initially set at 0.15 and 0.1 for momentum and pressure to facilitate convergence. Gradually increased after initial convergence until 0.5 and 0.4 for minimum error.

3.5.4 Running time

In order for the results to be accurate, the flow must be fully developed and each particle must have gone through the domain once. In this case this time will be determined mostly by the frequency of each case: at least one complete oscillation cycle is required to be completed before we can consider the data relevant. After that, the stabilization of the results is the main indicator for the development of the flow.

In practical terms, the total running time was determined by the queues related to the computational resources (calculation ran at the National Super Computer Centre at Linkping, Sweden), and were around one week of total running time for each case.

3.6 General project schedule

The first months of the project consisted on acquiring the required knowledge of the different tools required for the project. Several months were then spent on a different case that had to be dropped due to it not being technically feasible. Those months are not considered as part of this project.

For the current project, the creation of the mesh consisted of several trial and error iterations, where the mesh was changed according to preliminary data from the previous simulation each time. Most of the time dedicated to the thesis was spent in this part. Once a simulation was deemed good enough, data was extracted to be visualised with Ensight and MATLAB in detail.

A Gantt diagram of the schedule is shown below.

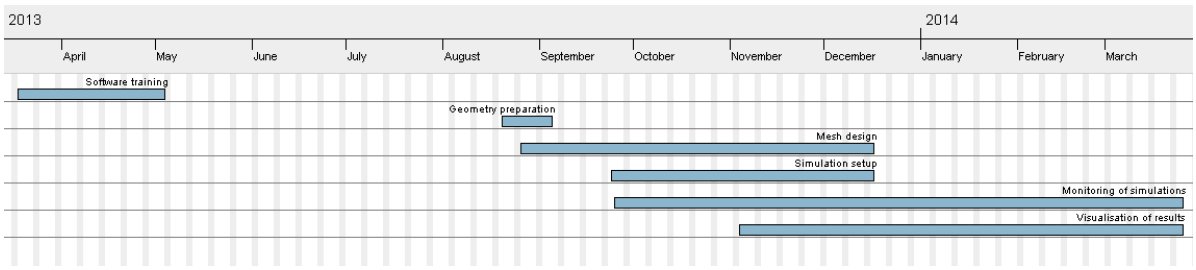

Figure 3.6.1: Gantt diagram of the project's workflow.

3.7 Economic study

3.7.1 Introduction

In this chapter a brief economic analysis of the project is done. Specifically, the costs related to it are calculated.

The total cost of the project is can be divided into two parts: direct and indirect costs. The first consists of salaries, amortisable material and non amortisable material. Indirect costs are related to services and administrative costs.

3.7.2 Direct costs

Salaries

In order to estimate the cost of the salaries related to this project, a number of working hours per years will be estimated.

Table 3.7.1: Yearly working hours

Concept	Days per year
Total	365
Weekends	104
Summer vacation	30
Holidays	9
Personal free days	8
Total working hours	210

If theere are 8 working hours per working day, this results in a total of 1680 working hours per year. Assuming a salary of 35000 euros per year, this means each working hours has a values of 20.83 euros.

The total number of hours dedicated to the project can be calculated form the Gantt diagram 3.6, considering that starting at september the working hours were reduced from 8 to 5 per day. This results in about 2008 working hours dedicated to the realisation of the project.

Table 3.7.2: Salary cost

Concepto	Value
Cost per hour (euros)	20.83
Number of hours [h]	2008
Salary cost (euros)	41826

Amortisable material costs

Main amortisable material in this project consists on hardware and software licenses. A linear amortisation approach will be considered here. It must be considered that license prices can vary greatly depending on the duration and volume of the package license, and also with different agreements that the company may have with the software developer. In the next table approximate values for one license and a duration of five years are considered.

Table 3.7.3: Software and hardware initial cost

Name	Cost [euros]
License for AVL Fire	8800
License for Ensight	1600
License for MATLAB	8000
License for Adobe Photoshop CS5	436
O.S. Red Hat Enterprise	217
Desktop computer DELL	1100
Laptop Surface PRO 2	899

Amortisation cost is what will be considered as porject cost related to this equipment and software. Hourly amortisation costs can be calculated as:

$$AmortisationPerHOur = \frac{InitialCost - ResidualValue}{TotalHours} \tag{3.7.1}$$

The residual value is considered zero for software and 5 % of the initial value for hardware (since some parts may be reused after the lifetime of the equipment). The total amortisation time is estimated to be 5 years, which translates into 8400 working hours. Hours of use for each element are extracted from the Gantt diagram.

Table 3.7.4: Amortisation of hardware and software (euros)

Name	Amort. cost per hour (euros)	Residual val.	Hours
License for AVL Fire	1.04	0.00	2000
License for Ensight	0.19	0.00	750
License for MATLAB	0.95	0.00	750
License for Adobe Photoshop CS5	0.05	0.00	10
O.S. Red Hat Enterprise	0.00	0.025	2000
Desktop computer DELL	0.12	55.00	2000
Laptop Surface PRO 2	0.10	44.95	400

Now the total amortisation cost for each piece of equipment can be calculated.

Table 3.7.5: Total amortisation costs

Name	Amortisation cost (euros)
License for AVL Fire	2080
License for Ensight	142.5
License for MATLAB	712.5
License for Adobe Photoshop CS5	0.5
O.S. Red Hat Enterprise	50
Desktop computer DELL	240
Laptop Surface PRO 2	40
Total	3265.5

Non-amortisable material costs

Non-amortisable material costs consist on things such as office material, printing, mailing...

Table 3.7.6: Non-amortisable material costs

Concept	Cost (euros)
Office material	120.00
Printing	200.00
Other	50.00
Total	370

Total direct costs

Here all sources of direct costs are added in order to obtain the total direct cost.

Table 3.7.7: Total direct costs

Concept	Total cost (euros)
Salaries	41826
Amortisable material costs	3265.5
Coste total de Non-amortisable material costs	370
Total direct cost	45461.5

3.7.3 Indirect costs

Indirect costs are usually smaller in comprison with direct costs and include explotation costs (electricity, phone...) and administrative and direction costs. These are detailed in the following table.

Table 3.7.8: Indirect costs

Concept	Total cost (euros)
Explotation costs	210
Administration and direction costs	290
Total indirect cost	500

3.7.4 Total costs

Finally, the addition of direct and indirect costs provides a final estimated cost for the project.

Table 3.7.9: Total costs

Concept	Total cost (euros)
Direct cost	45461.5
Indirect cost	500
Total cost	45961.5

This estimated total cost can be comapred to typical values that Chalmers charges for an study of this nature, around 20 euros per worked hour. however, this implies non-confidential results, and this value should be duplicated for confidential studies. Consider-

ing the 2008 hours worked in the proyect, this prices can be comapred with the estimated cost that has been calculated.

Table 3.7.10: Summary of total cost/price

Description	Value (euros)
Estimated cost of the project	45961.5
Price at 20 euros/hour (non confidential)	40160
Price at 40 euros/hour (confidential)	80320

Chapter 4

Results

Now the results of the different performed simulations are shown and analysed. The resolution requirements will be discussed in the first place, since the confidence in the quality of our results is greatly bound by them. Then some visualisations of the flow are presented around the body. Finally, the results for side force coefficient and z-axis moment coefficient are shown and compared to the experimental results.

4.1 Resolution

4.1.1 CFL number

The CFL number, as described in the Theory section, depends on both the cell size and the time step chosen for the simulation.

When the oscillating frequency is 4 Hz ($f = 0.7166$ for the scaled model) the CFL number is only below one for roughly the areas refined at level 0,1 and 2, which add up to about 12% of cells in the mesh. The rest of cells are in CFL values between 1 and 10, with about a thousand cells in the rear edge of the model reaching values as high as 50 (these cells represent around 0.007 % of the total number of cells). This indicates the selected timestep is still too large. However, due to time limitations this timestep could not be reduced further, and the mesh could not be made coarser in order to be able to reach convergence, especially in the rear edge and corners of the model.

The simulations for 2 Hz and 1 Hz had the timestep increased twice and four times respectively, so the CFL condition isn't reached in almost any cells. The convergence of none of the simulations was affected

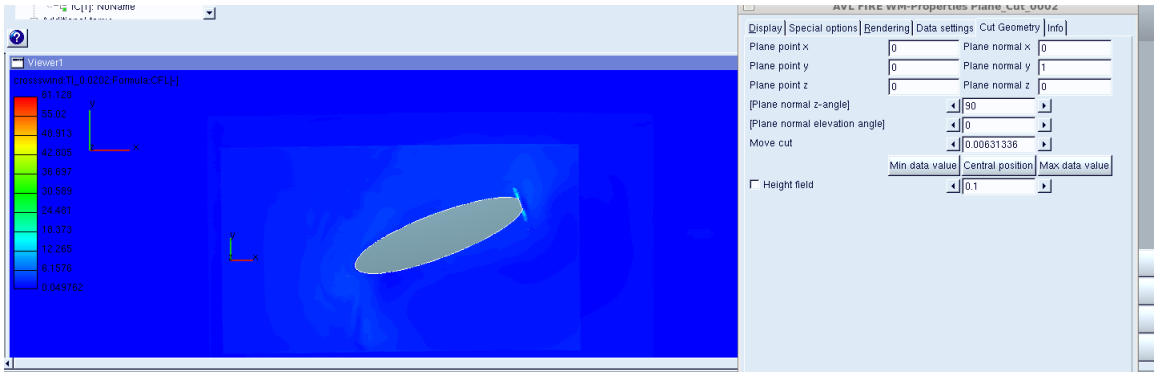

Figure 4.1.1: Z-Cut where the CFL number reaches higher values, for 4 Hz in a given time with the flow already developed.

4.1.2 Wall units

In order to completely resolve the turbulent scales, the resolution requirements discussed previously must be reached. The n^+ values are obtained directly for each cell from a userfunction introduced in AVL Fire Workflow. Since the dimensions of the cells in the boundary layer are known (their values have been specified in FAME Hexa when the mesh is produced), all the wall units can be obtained each time where 3D results where extracted. A summary of the results is presented below.

Unit	Maximum value	Apr. percentage of cells where requirement is not met
n^+	1.05	<0.1 %
s^+	47.25	< 1 %
l^+	47.25	0 %

Table 4.1.1: Resolution in term of wall units

Except for a very few cells , the resolution requirements for the the turbulence in the boundary layer are met. The results above are valid for the three simulations performed with almost no change, since the velocities in the boundary layer are of the same order and the mesh utilised is the same for all of them.

4.2 Flow visualizations

Some visualisations of the flow for the 4 Hz case are shown below. This was the case were the quality of the simulation, according to the resolution requirements are better. All results are shown for for different timesteps and positions for an enough developed flow. Note also that not all of the wind tunnel is represented, only the region of interest.

In Figure4.2.1 a Z-cut in the middle of the car model shows the magnitude of the velocities around the body and the extent of the wake behind it. Pressure distribution around the body is shown in figure 4.2.2.

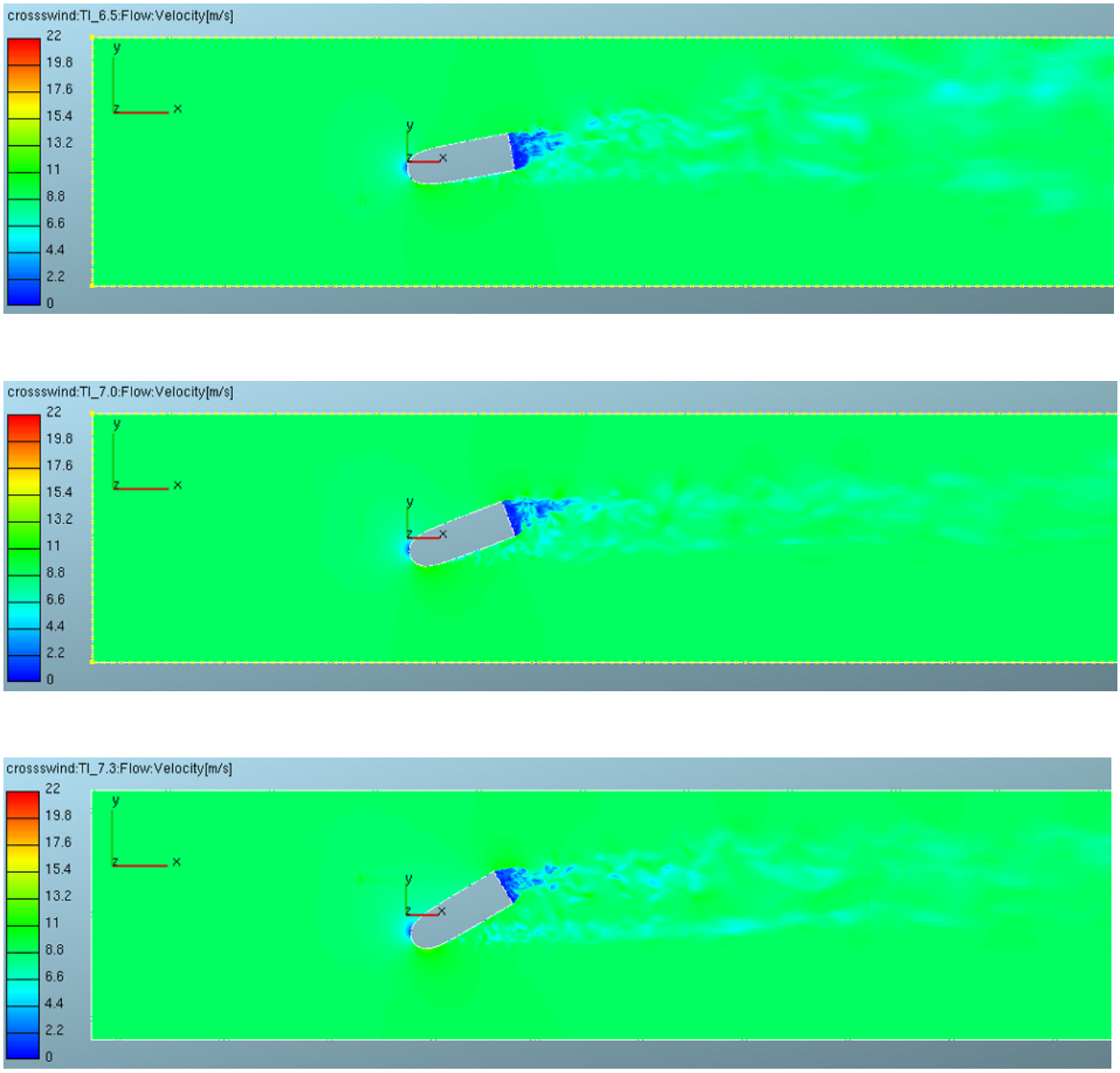

Figure 4.2.1: Flow velocity for a Z-cut in different points of the cycle (10, 20 and 30 degrees).

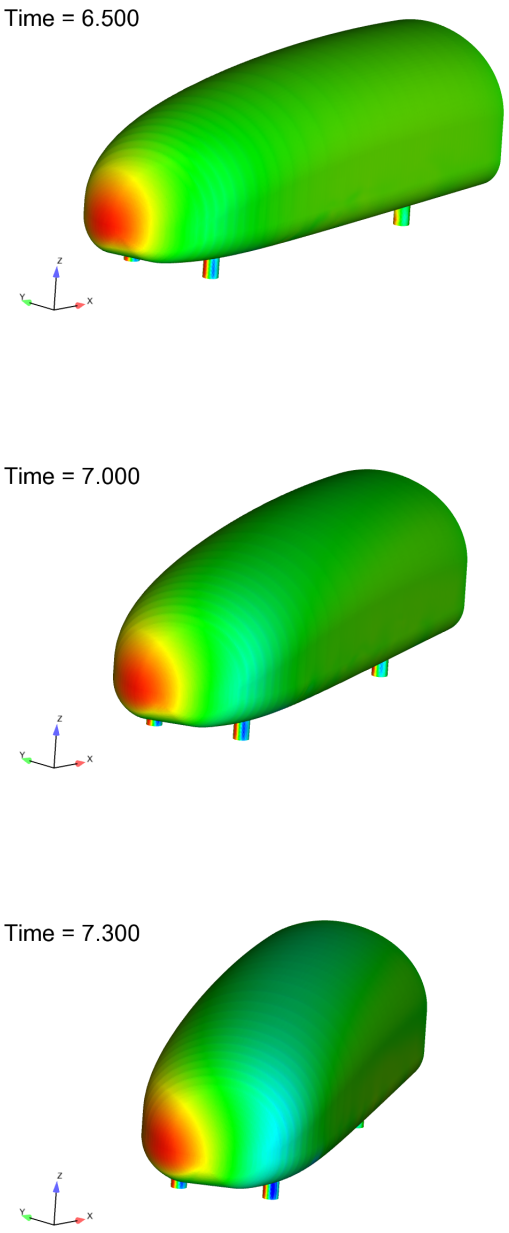

Figure 4.2.2: Relative pressure around the body for 10, 20 and 30 degrees positions.

The way in which the flow detaches from the body is visualised with tracing particles originating from the body. In figure 4.2.3 the results for three different positions of the body are shown are shown. At low incidence angle, the detachment happens mostly in the rear of the model as expected. For high angles, however, detachment of the flow is generalised also in the side opposite of the incoming flow.

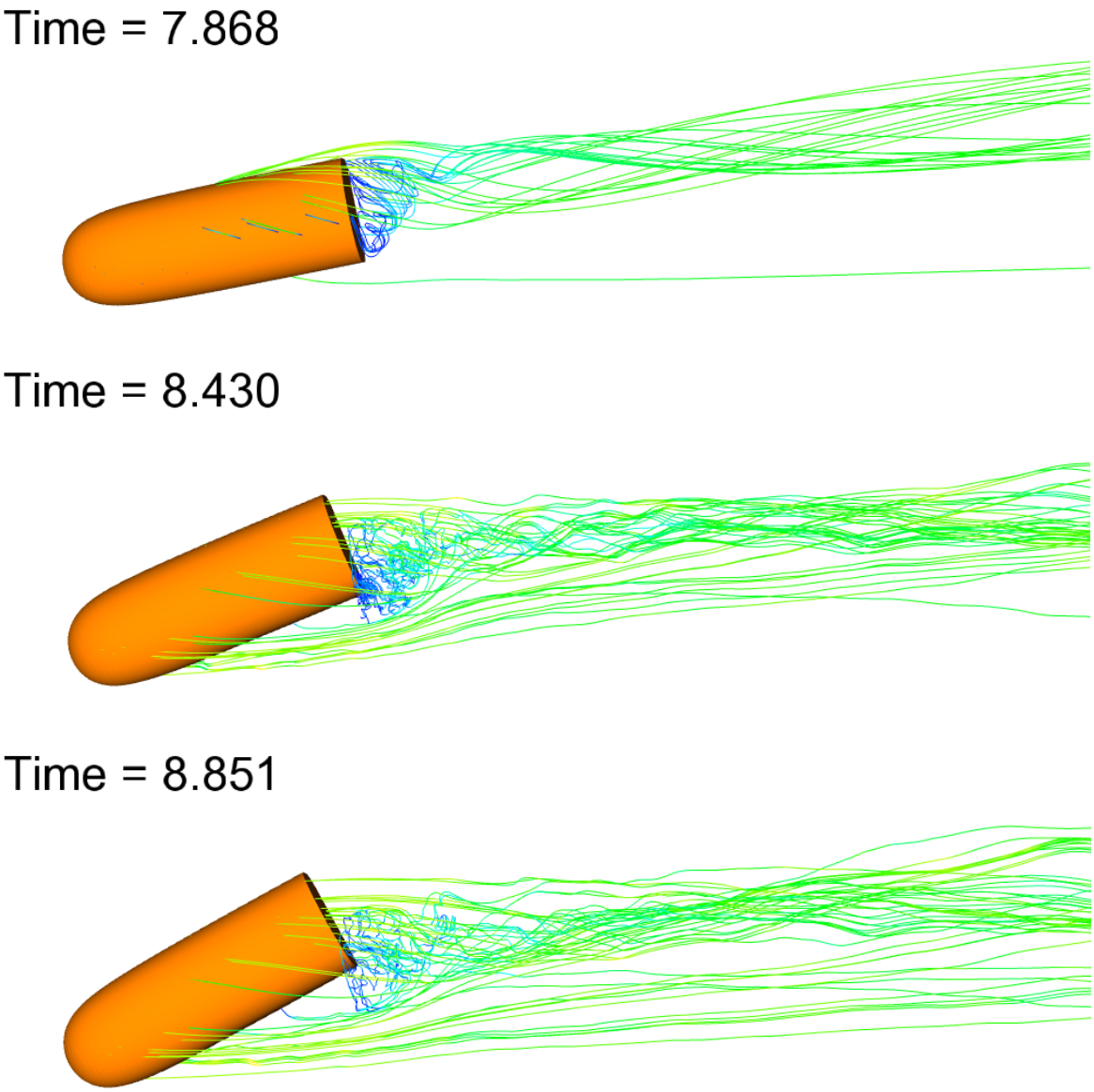

Figure 4.2.3: Flow detachment for different body position.

Additionally, the Q-Invariant of velocity can be used to visualise the characteristics of the turbulence around the body by rendering an isosurface of said magnitude. In order to observe the hysteresis effect (the different flow for the two halves of the cycle with the angle is increasing or decreasing), the same angle (19 degrees) is chosen, with a temporal separation of half a period.

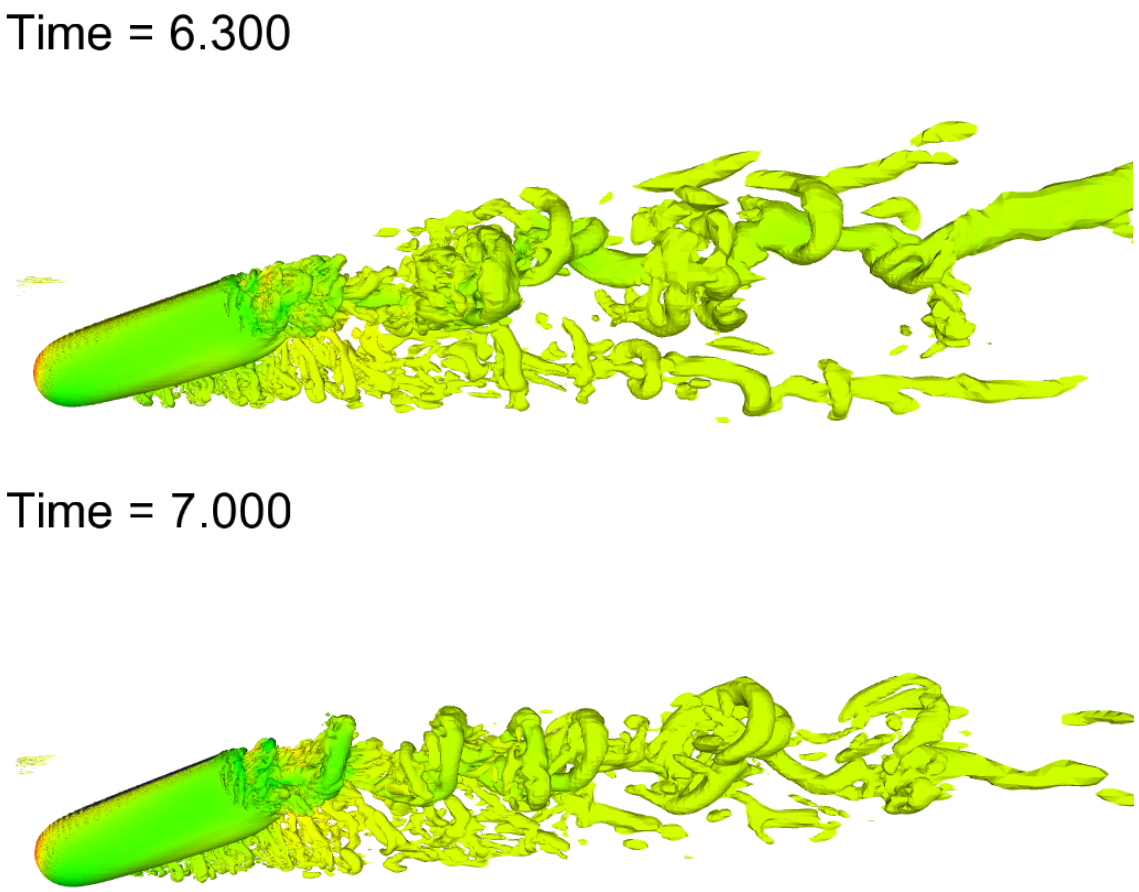

Figure 4.2.4: Velocity invariant Q=200 for the same geometrical position, for negative and positive angular velocities respectively.

It is drawn from 4.2.4 that, as expected from the experimental results, the behaviour of the flow is not only dependent in the position of the body (as you would expect when using a quasi-static approach), but also the previous history of the simulation. In this particular scenario, the effects of the inertia in the flow are clear: when the car model is reducing its angle relative to the flow, the turbulence behind it is following not instantaneously, but with a certain delay instead (note the extension of the wake in the positive Y direction). The opposite effect can be observed in the first picture of 4.2.4, where the angle is increasing instead.

4.3 Yawing moment and side force coefficients

The main two parameters to be compared with the experimental results are the yawing moment and side force coefficients for the model during an averaged cycle. The simulation results presented next are not averaged in time and represent three oscillation cycles after the flow was considered to be fully developed. Note that the direction of the cycles is counterclockwise for both magnitudes.

4.3.1 Model oscillating at 4 Hz

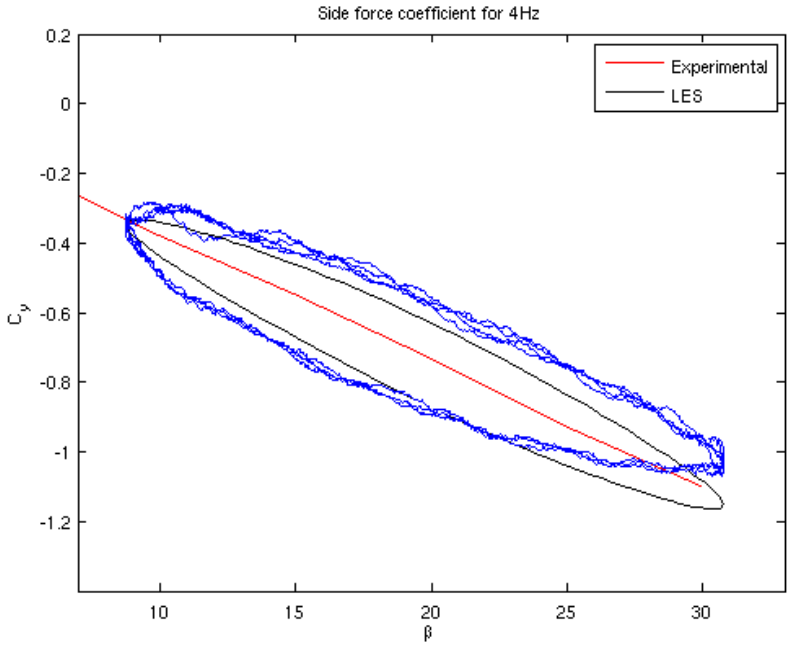

Figure 4.3.1: Side force coefficient for 4 Hz, LES and experimental.

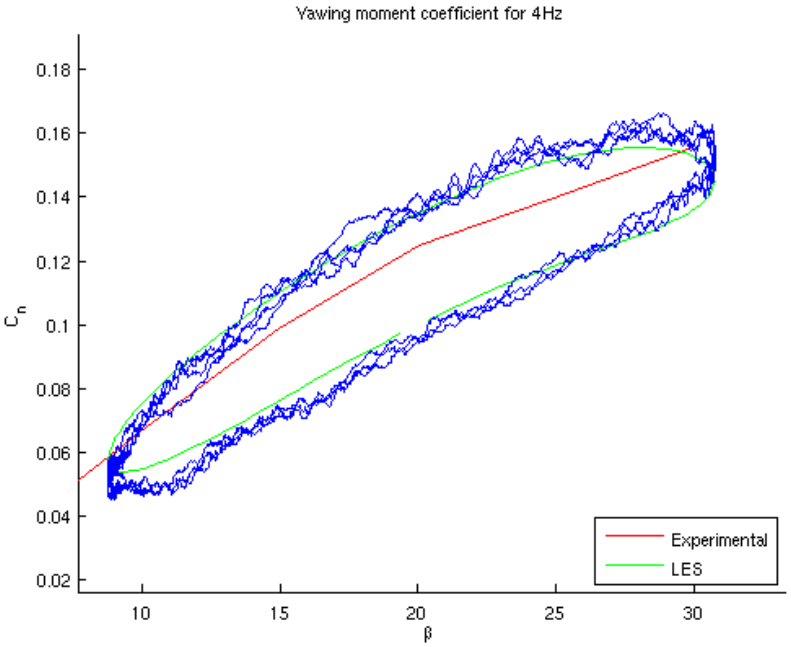

Figure 4.3.2: Yawing moment coefficient for 4 Hz, LES and experimental.

The simulation results succeed in capturing the hysteresis effect that the experiment revealed. This means that, for a given yaw angle, side force and yawing moment can have different values: one for each half of the cycle. Both the yawing moment coefficient and the side force increase when the yaw angle is increasing towards the most extreme position (wind reaching the model at 30). Also, as the rotation velocity is reduced towards the extremes of the cycle, the values get closer to the static measurements.

This indicates that the simulation can correctly reproduce the way on which the flow can't instantaneously follow the body when this is rotating. The hysteresis effect can be explained by observing the wake for different timesteps. When the rotation changes direction at 10 and 30, it takes some time for the flow to follow up due to the inertia associated to the flow. Thus the characteristics of the wake are different for each angle depending on the sign of the angular velocity.

The phase shift phenomenon is also present, defined here as the difference between the angle required to obtain the same coefficient on the dynamic and static case (or, in other words, the change of certain parameters for the same angle when going from quasiestatic approach to dynamic tests). This is closely related to the hysteresis effect. Since the flow structure around the body can't follow it with precision, there is always a different wake around the body to what would be expected from a fully developed and static situation.

However, the value of the coefficients doesn't fit the experimental results, with an error that increases with the angle, when the model is heavily rotated in relation to the direction of the incoming wind.

4.3.2 Model oscillating at 2 Hz

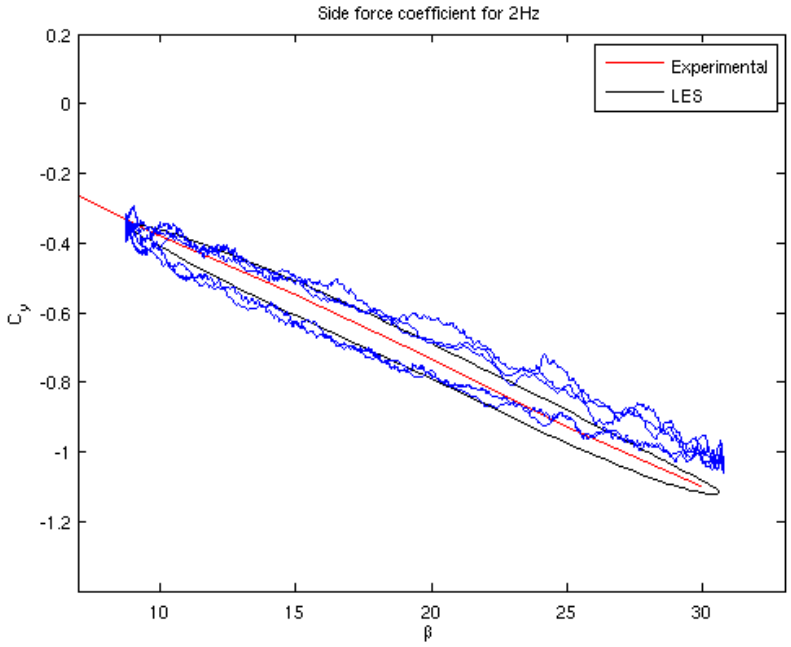

Figure 4.3.3: Side force coefficient for 2 Hz, LES and experimental.

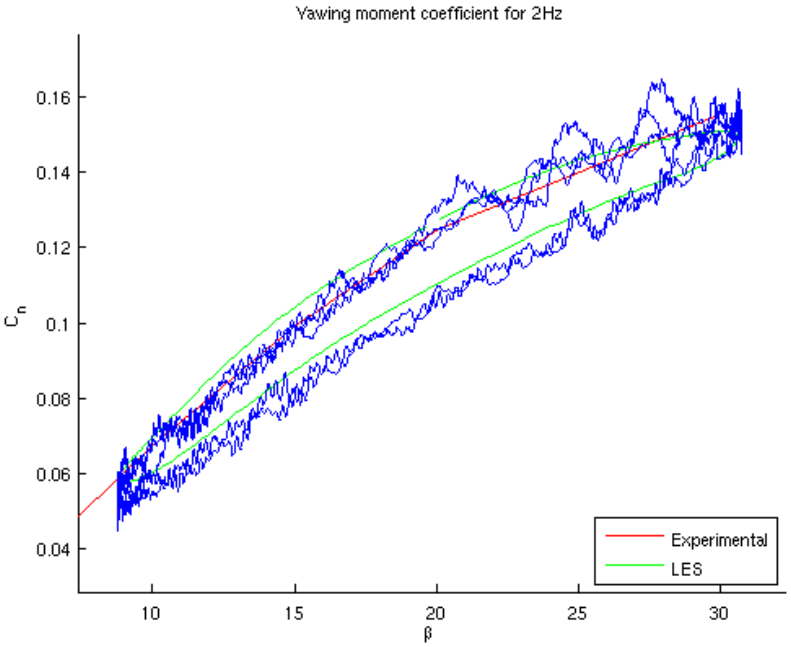

Figure 4.3.4: Yawing moment coefficient for 2 Hz, LES and experimental.

This time there are high oscillations in the simulation results that cause a higher error compared to the exprimental data. The increased timestep is reducing the accuracy of the results and the oscillations are very pronounced when close to 30.

However, the gap on the hysteresis cycle is reduced, as it should happen when the case get closer to the quasiestatic study.

4.3.3 Model oscillating at 1 Hz

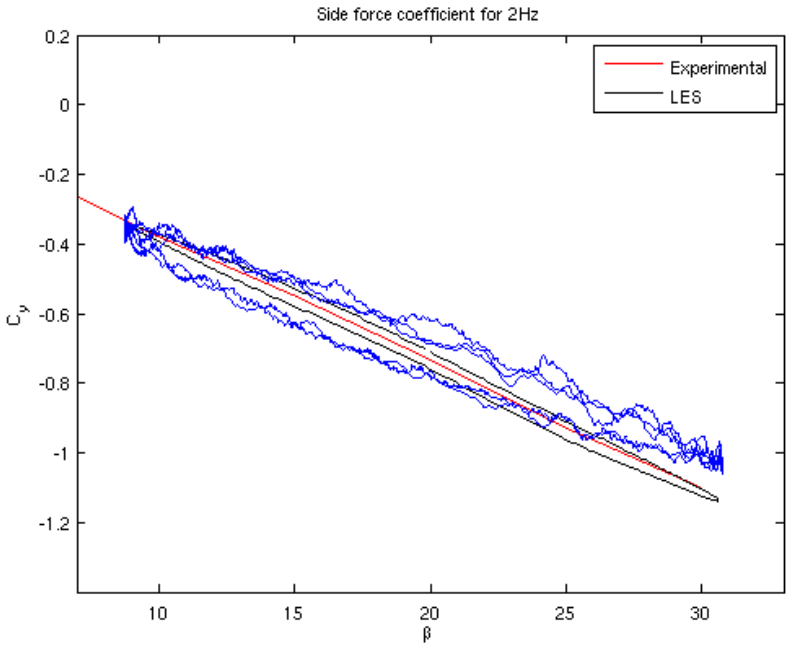

Figure 4.3.5: Side force coefficient for 1 Hz, LES and experimental.

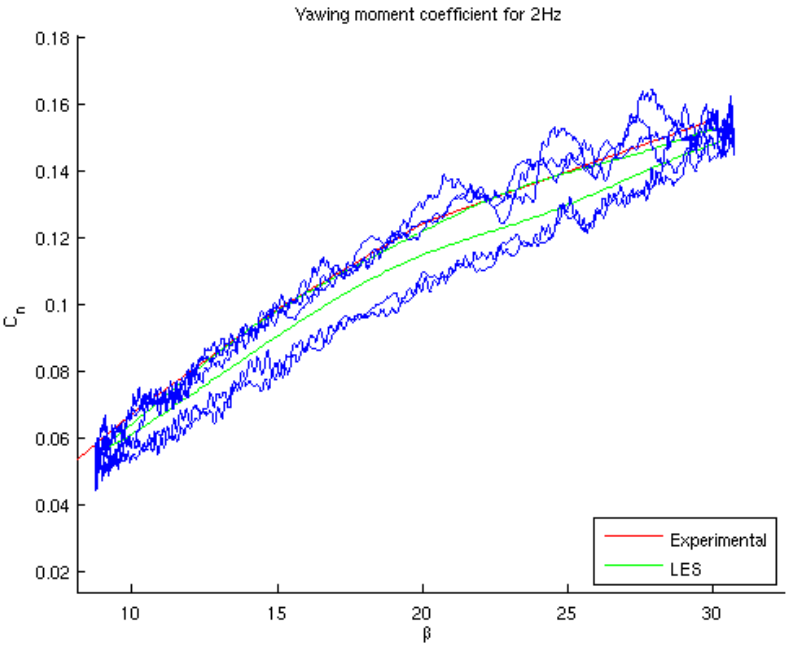

Figure 4.3.6: Yawing moment coefficient for 1 Hz, LES and experimental.

Finally, for the 1 Hz simulation, the quality of the simulation is clearly insufficient and the oscillations in the results are too high, although the average value and general behaviour of the results is maintained. The hysteresis cycle is closer to forming a simple line, since the flow can more easily follow a model rotating slowly.

4.4 Comparison with static LES and PANS simulations

In order to evaluate the influence of the dynamic deformation in the error between experimental setup and LES simulation, the 30 angle position was further studied. As observed in 1.2.3 and 1.2.4, in the experiment both the values for yawing moment and side force converge to a single value regardless of the frequency, even for the quasiestatic case.

If were the dynamic deformation of the mesh be the cause of this discrepancy, a simulation run with the model fixed at the 30 position should result in coefficients around the same values than in the experiments. In other words, the case of frequency equal to 0 Hz was simulated and compared to the experimental static results in order to narrow the source of error.

Furthermore, this simulation was run both with LES and PANS (Partially Averaged Navier-Stokes) models, in order to find if PANS may be a better alternative for this particular study.

The results of this test are exemplified in 4.4.1, for the highest frequency and side force coefficient.

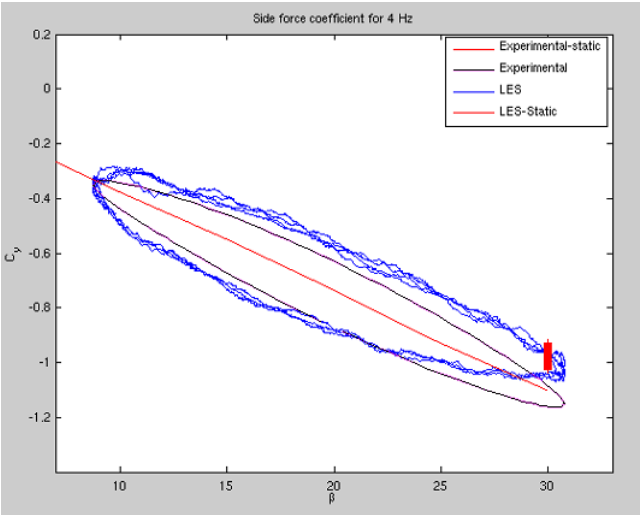

Figure 4.4.1: Comparison between static and dynamic experiments and simulations for 4 Hz.

The values obtained in the static simulation for 30 are in the same range than what would be expected if the simulation with the mesh being deformed at 4 Hz was correct. Thus the LES simulations are coherent among them, regardless if they are static or not.

The results for the static PANS simulation are slightly lower than for the LES, but this difference in neglectable compared to the magnitude of the difference between experimental and computational data (see 4.4.2). There is no reason then to believe that PANS would be a better alternative for this study.

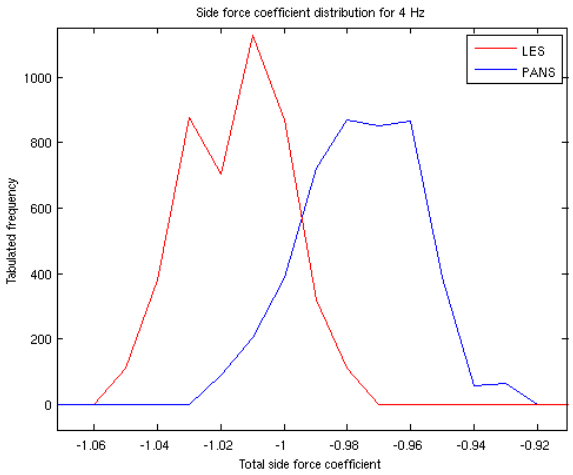

Figure 4.4.2: Distribution of the side force coefficient values obtained for the LES and PANS static simulations.

Chapter 5

Conclusions

5.1 Discussion of the results

The three main LES simulations succeeded in reproducing the effects that differentiate a quasistatic study of a changing flow compared to a more realistic, dynamic approach. Effects such as hysteresis and phase shift, that wouldn't appear as a result of the classical approach in CFD with static meshes and separate simulations, can be observed. This would lead to very different instantaneous values than expected. The way these phenomenons change with the frequency and yawing angle can also be qualitatively studied. It has been also evaluated that having a deforming mesh isn't a critical source of error by itself as long as the oscillation frequency isn't too high.

However, the values of the two main parameters studied in this thesis (side force coefficient and yawing moment coefficient) show clear quantitative differences with the experimental data. The hysteresis cycles are slighty wider for for coefficients (over and underestimation of the real value in corresponding parts of the cycle), and there is also an increased error for the force when the angle is close to 30.

Of the three simulations, the one realized for 4 Hz is the one with a better numerical simulation in terms of resolutions, even if it is still lacking, although convergence is not a problem and there isn't a visible difference in the main parameters when the timestep is decreased and allowed to run for an additional half cycle. Nevertheless, high oscillations were presents in the results that could only be reduced by lowering the blending factor to a value as low as 0.82. Further improvements required a more detailed mesh or, specially, further reduction of the timestep, which could not be done due to time and hardware restrictions.

The possibility that this difference in results could be due to the dynamic deformation of the mesh was tested by running a static LES simulation with the model fixed at 30 degrees. An equivalent simulation using PANS was also ran at the same time for this static case, in order to find possible differences between models. The results were similar for both simulations and resulted in values very similar to those obtained in the dynamic simulations.

It is thus concluded that for this particular case LES provides a very good description of the behaviour of the flow. However, a better mesh and a reduced timestep are most likely required to improve the precision of the results, especially when dealing with large incidence angles, where the turbulent wake becomes larger and thus the error associated with it.

5.2 Further work

Better understanding of the flow and the differences with the experimental results can be reached doing a longer simulation, with a higher number of cycles and a smaller timestep for a better averaging of results and a better resolutions. A geometry describing the wind tunnel in precision and considering blockage effects could also be used as a substitute to the one used in this work. The mesh could also be improved if it were to be made using a less automated, more versatile software such as ICEM CFD instead of FAME Hexa.

Annex I: Dynamic deformation code

The following code is insterted in AVL Fire Workflow Manager, ('Mesh deformation' section), in order to achieve the desired deformation of the mesh at each timestep. Given code is for the highest frequency case.

Global formula variables

```
double x0 = 0.33;
    double rMin = 0.39;
    double rMax = 0.7;
    double pi = 3.1415927;
    double positionFactor;
    double phit;
    double frequency = 0.7166651504;
    double midpoint = -0.24;
    double amplitude = 22;
```

Formula initialisation

```
positionFactor = (sin(2 * pi * frequency * t) + 1) / 2;
    phit = deg2rad(amplitude * positionFactor - amplitude/2 + midpoint);
    print "angle at t=", t, " is", rad2deg(phit);
```

Formula body

```
double phi, y[3] = x;
    double r = sqrt((x[0] - x0) * (x[0] - x0) + x[1] * x[1]);
    if(r < rMin)
    phi = phit;
    else if(r < rMax)
    phi = phit * (r - rMax) / (rMin - rMax);
    else
    return;
    x[0] = (y[0] - x0) * cos(phi) - y[1] * sin(phi) + x0;
    x[1] = (y[0] - x0) * sin(phi) + y[1] * cos(phi);
```

Bibliography

[1] Wikipedia. courant-friedrichs-lwey condition. 2014.

[2] F. N. Beauvais. Trasient nature of wind gust effects on an automobile. *SAE International Congress and Exposition, Detroit, MI, SAE*, 1967.

[3] L Davidsson. Fluid mechanics, turbulent ow and turbulence modeling, pages 131 to 138. 2013.

[4] R.G. Dominy and A. Ryan. An improved wind tunnel configuration for the investigation of aerodynamic cross wind gust response. *SAE INternational Congress and Exposition, Detroit, MI, SAE Paper no. 1999-01-0808*, 1999.

[5] V Ferrand and B Grochal. Dorces and flow structures on a simplified car model exposed to an unsteady harmonic crosswind.

[6] K. P. Garry and K.R. Cooper. Comparison of quasi static and dynamic wind tunnel-measurements on simplified tractor-trailer models. *J. Wind Eng. INd. Aerodyn. 22, pp 185-194*, 1996.

[7] Chometon F. Gilliron, P. and J Laurent. Analysis of hysteresis and phase shifting phenomena in unsteady three-dimensional wakes. *Exp. Fluids, 35, pp 117-129*, 2003.

[8] Chikhaoui O. DEng G. Guimineau, E. and M. Visonneau. Effect de vent lateral sur un mmodel simplifie de voiture par une methods des. *Mec. Ind., 10, pp 203-209*, 2009.

[9] E. Guimineau and F. Chometon. Experimental and numerical study of unsteady wakes behind an oscillating car model. *IUTAM Symposium on Unsteady Separated Flows and Their Control, IUTAM Book Series 14, pp. 367-379scillating Car Model*, 2009.

[10] H. Hemida and S. Krajnovic. Transient simulation of aerodynamic response of a double-deck bus in gusty winds. *SAE INternational Congress and Exposition, Detroit, MI, SAE Papaer No. 980392*, 2009.

[11] W..H Hucho and H J. Emmelmann. Theoretical prediction of the aerodynamic derivatives of a vehicle in cross wind gusts. *SAE INternational Congress and Exposition, Detroit, MI, SAE Paper no. 730232*, 1973.

[12] N. Kobayashi and Y. Yamada. Stability of one box vehicle in a croscross - an analysis of trasient aerodynamic forces and moments. *SAE INternational Congress and Exposition, Detroit, MI, SAE Paper no. 881878*, 1988.

[13] S. Krajnovic. Numerical simulation of the flow around an ice2 train under the influence of a wind gust. *International Conference ON Railway Engineering 2008 (IET ICRE2008), CHallenges for Railway Transportation in Information Age, Hong Kong, China, March 25-28*, 2008.

[14] S. Krajnovic and S. Sarmast. Numerical investigation of the influence of side winds on a simplified car at various yaw angles. *3rd Joint US-European Fluids Engineering Summer Meeting, Symposium on Issues and Perspectives in Ground Vehicle Flows, FEDSM-ICNMM2010-30766, Montreal,Canada-August 1-5*, 2010.

[15] M. A. Passmore and S. Mansor. The measurement of trasiet aaerodynamic using an oscillating model facility. *SAE INternational Congress and Exposition, Detroit, MI, SAE Papaer No. 2006-01-0338*, 2006.

[16] J. Smagorinsky. General circulation experiments with the primitive equations. *Mon. Weather Rev., 91(3), pp 99-165*, 1963.